Size effects on the fracture behavior of amorphous silica from molecular dynamics simulations

Raúl Barciela [a], Thiruvilla S. Mahadevan [b], Félix Quintero [a,*], Juan Pou [a], Jincheng Du [b]

[a] CINTECX, Universidade de Vigo, LaserON research group, E.E.I, Vigo, 36310, Spain
[b] Department of Materials Science and Engineering, University of North Texas, Denton, TX 76203, USA

ARTICLE INFO

ABSTRACT

In this work, the role of structure size and interaction potential on the ductility and mechanical properties of bulk glasses are extensively analyzed using molecular dynamics (MD) simulations. Elastic moduli and mechanical properties for bulk silica structures were calculated from the MD trajectories using three different force fields - diffusive charge reactive potential (DCRP), Teter and Vashishta potentials. These results from MD simulations were compared to experimental measurements and the overall results reassert that, while the elastic moduli show a neglectable variation with structure size, the fracture behavior is considerably affected. Specifically, it is found that the length along the deformation axis is the driver for the brittle to ductile transition. The fracture results, combined with an energy analysis, reveal that the energetic condition for brittle fracture, where elastic strain energy should overcome the fracture surface energy, remains valid for the three potentials.

1. Introduction

Glass is widely accepted as a brittle material at room temperature. However, some experimental studies reveal evidence of ductile behavior of bulk glasses at room temperature. Particularly, electron beam radiation is shown to activate viscoplastic deformation processes at room temperature [1–3]. Furthermore, plasticity has also been observed without the electron beam irradiation. Indeed, ductile behavior was observed on silica glass upon cold compression [4]. Also, evidences of ductile flow have been observed in the nanoscale near the crack tip during glass deformation, which resembles the behavior involved in ductile fracture in the microscale [4,5]. On the other hand, a brittle to ductile transition has been observed during tensile tests of amorphous silica nanofibers when the diameter is lower than 10 nm [6]. Uniaxial tensile tests, based on the measurement of the stress-strain curve, are a common technique for determining the Young's modulus and breaking behavior of materials. In the case of micro- or macroscale tensile experiments without irradiation, the stress-strain curve of glasses usually resembles that of a brittle fracture, showing a linear elastic zone up to the maximum stress followed by a sharp fall to zero in the stress [7], despite the evidence of ductility observed in the nanoscale at the vicinity of the crack tip.

Atomistic simulations are often used to study glasses and crystalline materials. Molecular Dynamics (MD) simulations have been shown to be a useful tool to extract valuable structure-property relation information in various oxide glasses that can be difficult to obtain experimentally. In this regard, the choice of an adequate interatomic potential is essential for the success of MD simulations and, as a result, different interatomic potentials have been developed over the years to assess different properties of glasses [8–11]. MD simulations have been widely used to study the mechanical behaviors and elastic properties of silica and silicate glasses. There are multiple potentials such as the BKS potential [12,13], the PMMCS potential [14–16], the SHIK potential [17,18], which all share the common feature of partial atomic charges with pairwise interactions, and more complex ReaxFF potential [19,20] which is bond order based with charge equilibration, that have been developed and some used for the modeling of mechanical properties and deformation of silica (and silicate) glasses. However, a matter of debate has always been whether MD simulations are able to mimic the brittle fracture of glasses or either explain some of the evidence of plastic deformation observed in experiments. Indeed, tensile testing with MD simulations of bulk silica glass can result in a ductile breaking behavior, as evidenced from the large ductile tail in the stress-strain curve observed after the maximum stress is reached, which does not represent the typical brittle fracture of glasses [12,15]. For this reason, a deeper analysis of the deformation process, in order to clarify the mechanisms involved in MD tensile

simulations, is needed. Here we first examine several studies of MD simulations of fracture of silica glasses reported in the literature.

Some works attempted to understand the mechanisms involved in the deformation process of glasses from the point of view of MD simulations. Pedone et al. studied the deformation process of bulk silica glass by performing tensile MD simulations and they showed the presence of two different regions [15]. The first region corresponds to the elastic region. In this region, the deformation was shown to be due to an increase of the Si—O—Si angle at low strain and a stretching of the Si—O bond length at higher strains. In this region, a non-linearity of the Young's Modulus is observed, with a hardening of the structure in the first steps of the elastic zone, while decreasing during the second part of the curve. This non-linearity is presumably due to the anharmonic term of the potential and has also been observed in experiments [21]. In the second region, the Si—O bond breaking events get started. The third region corresponds to the unstable region, where voids are generated and grow rapidly with the strain which leads to the structure break. In the third region, a considerable ductility is observed.

Wang et al. performed MD simulations to study the mechanisms of crack propagation and their correlation with the stress-strain curve in bulk silica glass and calcium aluminosilicate glasses [22]. They observed that bulk silica glass showed a brittle behavior, as revealed from the sharp fall in the tensile curve and the rapid increase of the crack radius upon reaching a critical strain.

The residual ductility and localized necking observed in simulations has been considered as an artificial ductility which arises from mechanisms that are inherent from MD simulations [12]. Indeed, structure size has been shown to have a considerable effect on residual ductility observed in MD simulations [12,23]. Accordingly, Yuan et al. proposed that structure size effects may be the origin of the observed ductility in the third region, while no size effects have been observed at the elastic and yield regions [12]. They performed MD tensile tests using BKS potential and proposed that the system length along the deformation axis may have a major effect on the system ductility. They estimated a ductile to brittle transition at a system length of 10 nm. An energetic approach was used to explain this change and they proposed that a condition to have a brittle behavior is that elastic strain energy should be higher than fracture surface energy [12].

On the other hand, mechanical properties in the elastic region have also been studied through MD simulations using different potentials via calculation of the stiffness matrix or from MD tensile deformation tests. BKS potential has been widely used in MD simulations of mechanical properties and the Young's Modulus was analyzed from the resulting stress-strain curve, revealing a significant dependence on the short range cutoff of the potential, ranging from 84 GPa, at 5.5 Å, to 71.8 GPa, at 10 Å [12,13]. MD simulations of uniaxial tensile tests performed by Zhang et al. resulted in a Young's Modulus of 58 GPa using reaxFF potential [20]. Luo et al. obtained a Young's Modulus of 109 GPa from MD tensile tests of fibers using Vashishta potential [6]. However, pairwise empirical potential developed by Pedone et al. has provided the most accurate modelling of the mechanical properties, obtaining a Young's Modulus value of 69.9 GPa from MD tensile deformation tests of silica glass [15]. This value is closed to the experimental Young's Modulus for silica glass of 72.5 GPa [24].

However, even though some potentials have successfully modelled the mechanical properties of glasses, few works analyzed the size effects on the ductile processes observed in MD simulations of mechanical tests. Specifically, the extent of the conclusions towards extended structure sizes and different potentials remains unanswered. Therefore, a more complete analysis of the structure size effects on the observed ductility and its dependence on the interaction potential is needed.

The above-mentioned gaps are stimulated by the recent development of potential parameters by Deng and Du for borosilicate and aluminosilicate glasses [8], which enable MD simulations of these glasses whose mechanical properties remain unexplored. The development of these potentials has been motivated by the growing interest on borosilicate

glasses in applications as immobilization of nuclear waste, optical components or fiber glasses, which stimulated the development of several interatomic potentials for these systems and where the study of their mechanical properties is of special concern [8–10,25]. This includes the Teter potential, a partial charge pairwise potential for silica and silicate glasses initially parametrized by D. M Teter and later improved by Du and Cormack [26–28]. This was further expanded to give it the capability to model multicomponent aluminosilicate and borosilicate glasses [8]. On the other hand, the quest to model glass surfaces in wet atmospheres led to the development of potentials attempting to model glass-water interactions in glass interfaces. Particularly, the diffusive charge reactive potential (DCRP), initially developed by Mahadevan and Garofalini [29] for water silica and expanded later by Mahadevan, Du and other others [30], has the capability to study the glass-water interactions in silica and aluminosilicates with a high computational efficiency [31]. The analysis of the mechanical properties resulting from this potential is of special interest as it has the capability to model the effect of a moist environment on crack propagation velocity and its impact on the mechanical properties [32,33].

Here, we analyze the size effects on deformation behavior of bulk amorphous silica glass from the point of view of MD simulations. For this, we analyze the ductility and its dependence on the interaction potential by choosing three different potentials with unexplored mechanical properties. These include the recently developed interaction potentials, partial charge pairwise Teter potential with recent expansion by Deng & Du [26,27] and the DCRP [29,31]. The third potential involves the Vashishta potential, which was one of the earlier interatomic potentials with partial atomic charges and pairwise and three-body interactions parameterized for silica glass and showed to be able to generate silica glass structures in good agreement with experiments such as neutron diffraction and vibration density of states [11]. The choice of the three potentials used in this work is also due to the fact that they provide possibility of expanding the work to multicomponent glasses (Deng & Du potential) [26,27], to simulate glass-water interactions (DCRP potential) [29,31] and to test the effect of three-body interactions (Vashishta potential) [11] on fiber glass simulations. Also, this work provides a comparison of the mechanical properties obtained from the calculation of the stiffness matrix and from MD tensile deformation tests with respect to experimental results. The results are compared against other results from other potentials existing in the literature.

The study is divided in the following parts. In Section 2, the computational approach is presented. For this purpose, in Section 2.1, the simulation procedure to obtain the glass structures following the three potentials is included. In Section 2.2, the two methods to compute the elastic moduli are presented. Section 2.3 provides details about the MD simulations of uniaxial deformation processes. Finally, in Section 2.4, the energy considerations to analyze the size effects on glass ductility in MD simulations are presented.

In Section 3, the results are presented. In Section 3.1, a preliminary structure analysis of the quenched structures is included. In Section 3.2, the structure size effects on system ductility are assessed and explained from the point of view of the energetic analysis. Then, in Section 3.3, the elastic moduli and mechanical properties are presented and compared to that obtained from other MD simulation works and the experimental values of amorphous silica glass.

2. Computational process

2.1. Simulation procedures

MD simulations of bulk amorphous silica structures were performed using the large-scale atomic/molecular massively parallel simulator (LAMMPS) package [34] using three different potentials: DCRP [26,27], Teter [29,31] and Vashishta [11] potentials. Bulk silica structures were generated following a melt quench approach. The structures where initially melted to 6000 K for 20 ps in an NVT ensemble (constant

number of atoms, volume, and temperature). Then, they were cooled continuously to 300 K with a cooling rate of 5 K/ps.

The instability of Vashishta potential during NPT cooling at 1 bar led to consider alternative routes involving higher pressures to avoid such instability. Therefore, the NPT step of the cooling process was performed considering two pressure routes: one with ramping pressure from an initial pressure of 100 bar and linearly decreasing to 1 bar at 300 K and one with constant 1 bar pressure during cooling.

The 100 bar cooling route consists of an initial NVT ensemble until 3600 K followed by an NPT (constant number of atoms, pressure, and temperature) ensemble up to 300 K. For DCRP potential, the transition was done at 1300 K. The NPT step was performed from an initial pressure of 100 bar, linearly decreasing to 1 bar at 300 K. Then, at 300 K, two subsequent equilibration steps of 100 ps at a constant pressure of 1 bar and 100 ps at constant energy were performed.

Conversely, the 1 bar route involves an initial NVT step starting from an initial temperature of 6000 K to final temperatures of 1000 K and 3000 K, for DCRP and Teter, respectively. Then, an NPT step at a constant pressure of 1 bar is performed to a final temperature of ensemble up to 300 K. For, Vashishta potential, the cooling process was performed in a single NVT step from 6000 K to 300 K. Finally, for the three potentials, at 300 K, two steps of 100 ps at a constant pressure of 1 bar and 100 ps at constant energy are also performed.

Nosé-Hoover thermostats and barostats were used in the three potentials to control pressure and temperature [35–37]. A fixed timestep of 1.0 fs was used for the MD simulations.

The final densities estimated for bulk structures of 15,972 atoms generated following DCRP, Teter and Vashishta potentials yield values of 2.327 g/cm^3, 2.359 g/cm^3 and 2.565 g/cm^3 at the 100 bar pressure route, which are appreciably higher than the experimental value obtained for amorphous silica of 2.2 g/cm^3 [24]. At the 1 bar pressure route, DCRP results in a density of 2.205 g/cm^3, which is more similar to experiments. Conversely, for Teter and Vashishta, the calculated densities at 1 bar yield values of 2.329 g/cm^3 and 2.551 g/cm^3, which are slightly lower than that obtained at the 100 bar route.

In order to explore the size effects on the deformation behavior during uniaxial tension MD simulations of bulk glasses, bulk structures with different sizes and geometries were tested. For this purpose, a systematic analysis was performed following a two factor approach, involving the cross section effect as a first factor, and the geometry effect as a second one. Considering that the deformation takes place in z direction, the former was defined by the l_x edge length, while the latter was defined by the l_z length to l_x ratio.

Five different levels for the l_x edge length and four levels for the l_z/l_x ratio where considered, with nominal values of 3.5 nm, 5.5 nm, 7.5 nm, 9.4 nm and 10.9 nm for the first one, and 0.75, 1.4, 2.8 and 4.2 for the second, respectively.

The set of all the possible combinations of different values of the two factors where considered. In Table 1, the different combinations and their corresponding number of atoms and final density and dimensions after the melt-quench process are shown for DCRP potential and the previously described 100 bar pressure route. The final values corresponding to Teter and Vashishta potentials are shown in Table S1 and Table S2.

2.2. Elastic moduli

The elastic moduli, including bulk (*B*), shear (*G*) and Young's modulus (*E*), and the Poisson ratio (*ν*), were calculated via a static method involving energy energy minimization. For this purpose, the components of the stiffness matrix, *Cijkl*, were estimated using MD simulations. The stiffness matrix is obtained from the second derivative of the energy with respect to the strain ($C = \frac{1}{V}\frac{\partial U}{\partial \varepsilon \partial \varepsilon}$). Then, the components of the compliance matrix, *Sij*, are obtained from the stiffness matrix as $S = C^{-1}$. For the calculations of the elastic moduli from the

Table 1
Final density and dimensions of silica structures obtained with DCRP potential at the 100 bar pressure route.

Combination value		Number of atoms	Final melt-quench structure			
l_x / nm	l_z/l_x		Density /g·cm^{-3}	l_x / nm	L_y / nm	L_z / nm
3.5	0.75	2352	2.329	3.479	3.479	2.774
3.5	1.4	4116	2.333	3.477	3.477	4.853
3.5	2.8	8232	2.331	3.478	3.478	9.709
3.5	4.2	12,348	2.324	3.482	3.482	14.580
5.5	0.75	8712	2.318	5.476	5.476	4.169
5.5	1.4	15,972	2.329	5.467	5.467	7.631
5.5	2.8	31,944	2.324	5.471	5.471	15.270
5.5	4.2	47,916	2.328	5.468	5.468	22.890
7.5	0.75	21,600	2.329	7.455	7.455	5.550
7.5	1.4	40,500	2.329	7.455	7.455	10.400
7.5	2.8	81,000	2.327	7.457	7.457	20.820
7.5	4.2	121,500	2.325	7.459	7.459	31.230
9.4	0.75	43,320	2.333	9.438	9.438	6.930
9.4	1.4	82,308	2.327	9.445	9.445	13.180
9.4	2.8	164,616	2.327	9.445	9.445	26.370
9.4	4.2	246,924	2.328	9.445	9.445	39.550
10.9	0.75	63,888	2.323	10.944	10.944	7.638
10.9	1.4	127,776	2.328	10.936	10.936	15.263
10.9	2.8	255,552	2.327	10.938	10.938	30.533
10.9	4.2	383,328	2.326	10.939	10.939	45.805

compliance matrix, the Voigt, Reuss and Hill average methods were considered. Voigt method assumes that the strain is uniform over the aggregate while Reuss method assumes a constant stress. Hill's method calculates the mechanical properties as an average of the values obtained using Voigt and Reuss methods [38].

The Young's Modulus was also compared to that obtained by direct analysis of the curves, after the stress-strain curves were generated. In MD simulations of tensile tests of glass structures, the elastic region usually presents a strong nonlinear behavior, which can be explained by the strong nonlinear behavior of silica glass shown in experiments [15, 21]. Indeed, it was found from MD simulations of pure silica glass, the tangent modulus increases with strain and reaches a maximum at around 10 % strain, with a subsequent decrease [12,15,18,21,39]. Considering this behavior, the Young's Modulus is computed considering different fitting ranges of the deformation curve. On the other hand, a fit of the stress-strain curve in the elastic region is performed according to a 3rd order polynomial.

$$\sigma(\varepsilon) = E_0\varepsilon + \left(\frac{E_1}{2}\right)\varepsilon^2 + \left(\frac{E_2}{6}\right)\varepsilon^3 \tag{1}$$

Such expression allows to estimate the tangent modulus at different strains, which can be obtained as:

$$E(\varepsilon) = E_0 + E_1\varepsilon + \left(\frac{E_2}{2}\right)\varepsilon^2 \tag{2}$$

Where E_0 is the zero-strain Young Modulus.

2.3. Uniaxial deformation tests

Uniaxial tensile tests were conducted in the different bulk configurations with the three potentials. Deformation was performed in z direction at a constant strain rate of 10^9 s^{-1}. Multiple works have studied the role of the selected statistical ensemble (NVT or NPT) in the lateral axes during the deformation on the mechanical properties and structure breaking behavior [15,16,18].

In NVT ensemble, structure dimensions orthogonal to the deformation direction remain fixed during the deformation, while NPT ensemble allows the lateral atoms to relax in a fixed pressure. NVT usually promotes a brittle breaking behavior, as a tri-axial tension state is imposed in the system [15,16,18]. Conversely, NPT ensemble results in increase

of the fracture strain, due to the release of the lateral tension stresses. Recently, Zhang et al. compared MD simulations of uniaxial tensile tests of pure amorphous silica under NVT and NPT conditions, observing an increase of the Young's Modulus and a considerable decrease of the fracture strain when NVT is used [18]. Therefore, there is a general agreement that the choice of the statistical ensemble (NVT or NPT) has a significant influence on the deformation results.

However, NPT ensemble may provide a more realistic analysis of glass deformation in experimental tensile tests, which generally impose a uniaxial tensile stress, while keeping the lateral axes free to move at a fixed pressure (i.e. atmospheric pressure). Conversely, the fix of the cross section during the deformation, as in NVT ensemble, does not represent a realistic modelling of the deformation in glasses in experimental conditions, while also limits the possibility of ductile processes. Therefore, in the aim to understand the breaking behavior of glasses in experimental conditions, the use of NPT ensemble may provide more realistic fracture behavior [15,16,18].

Therefore, here, deformations were performed on a NPT ensemble at 300 K and 1 bar allowing therefore the lateral atoms to relax. The real stress was then calculated by dividing the sum of stresses of all the atoms by the instant volume. Then, an engineering stress was obtained by correcting the real stress by the relation between the instantaneous cross section and the initial one, A/A_0.

2.4. Energy considerations

It has been shown that energy considerations can provide a meaningful explanation of the size effects on deformation behavior of glass structures during uniaxial deformation tests [12,22,23]. Indeed, it has been shown that the fracture behavior can be explained in terms of a balance between fracture surface energy and elastic strain energy [12].

Potential energy of the structures at a certain point of the deformation can be obtained from the stress-strain curve as:

$$PE = l_x l_y \int \sigma_z \mathrm{d}l_z \tag{3}$$

Where $l_x l_y$ is the initial structure cross section and σ_z is the engineering stress.

Potential energy during the deformation has the contribution of an elastic energy and a surface energy. Before any axial deformation is applied, the structures are fully relaxed, and their potential energy is 0. As the deformation starts, potential energy increases in terms of elastic energy while fracture energy is neglectable at the first steps of the deformation. As the crack grows and starts to propagate, elastic energy releases progressively into surface energy. When the structure break occurs, elastic energy is fully released, and potential energy contribution comes only from surface energy. Therefore, total fracture surface energy (defined as the energy needed to create a new surface by fracture) can be estimated as the change of the potential energy at the end of the deformation process with respect to that of the relaxed structure. Since, MD deformations are performed at a fixed temperature of 300 K, such definition of total surface energy includes isothermal relaxation after the fracture and it can be estimated from the integration of the previous expression all over the whole deformation process [23]:

$$FSE_{\mathrm{relaxed}} = l_x l_y \int_{L_0}^{L_f} \sigma_z \mathrm{d}l_z \tag{4}$$

Relaxed fracture surface energy, γ_f, is defined as the energy needed to create a unit area of new surface by fracture:

$$\gamma_{\mathrm{f,relaxed}} = \frac{FSE_{\mathrm{relaxed}}}{2A} \tag{5}$$

Where A is the crack surface area at the end of the fracture.

Another approach to estimate fracture surface energy consists of estimating an unrelaxed total fracture surface energy, $FSE_{\mathrm{unrelaxed}}$, where the structure is forced to break without any structural relaxation. For this, two perfectly flat surfaces were created by inserting a gap of 50 Å in z dimension without any structural relaxation. Then, fracture surface energy is calculated as the difference between potential energy before inserting the gap and after inserting the gap. $FSE_{\mathrm{unrelaxed}}$ usually yields higher values, as it defines an upper bound for ideal fracture with perfectly flat surfaces.

$FSE_{\mathrm{unrelaxed}}$ provides an estimation of the energy change provided that a perfectly brittle fracture occurs in the sample. On the other hand, relaxed fracture surface energy, $\gamma_{\mathrm{f,relaxed}}$, is challenging to estimate because of the surface roughness of the created surfaces, while $\gamma_{\mathrm{f,unrelaxed}}$ is more direct because the created surfaces present no roughness [22]. Therefore, in this work, FSE and γ_f are calculated without any structural relaxation.

On the other hand, elastic strain energy, ESE, was computed from the area under the stress-strain curve in the elastic region, which was approximated as:

$$ESE = \frac{1}{2} E \varepsilon^2 \; l_x l_y l_z \tag{6}$$

where E is the Young's Modulus evaluated at the 0–3 % strain range and ε is the elastic strain limit. Usually, elastic region is usually delimited by the yield point, which is defined as the point of the stress-strain curve which leads to a non-recoverable strain of 0.2% when the stress is released. However, in tensile MD simulations, glasses are observed to show a strong non-linear behavior, which makes this approach an unrealistic definition of the elastic limit. As a result, on the view of the deformation curves, elastic strain limit is taken conventionally as 10 % and 15 % for DCRP and Teter potentials. For Vashishta potential, elastic strain limit is taken as 12 %, as used in previous studies [15,16,20].

3. Results

3.1. Structure analysis

SiO$_4$ tetrahedra are the main structural units in silica glass and link each other through corner-shared oxygen. The structure analysis in the short range order involves the study of the SiO$_4$ tetrahedron, which consists of the determination of the Si—O bond distances and the O—Si—O angles, while the intermediate order is concerned with the interconnection and relative orientation between units and the network topology. For the computation of the structure properties, a structure with 15,972 atoms was considered, in order to stay well above the minimum system size of 10^3–10^4 atoms, therefore to avoid fluctuations and obtain reliable structural information and elastic moduli of glasses [40].

The structures generated using the three potentials have been validated from the comparison of the structure factors (S^N (Q)) and total correlation functions (T^N (r)) generated with MD simulations against neutron diffraction experimental results. As shown in Fig. 1, the structure factors in the higher reciprocal space do not show a noticeable dependence on the potential and they agree with neutron diffraction data. At the lower reciprocal space, the diffraction peak positions and intensities significantly agree with the experimental data for DCRP and Teter potentials, while slightly lower intensities are obtained for Vashishta potential. The total correlation functions also indicate a reasonable agreement with the experimental data, as confirmed by the low R_x factors obtained from the fit of the three potentials to the experimental curves (7.7 % for DCRP, 6.7 % for Teter and 8.5 % for Vashishta).

Information about the short and intermediate order of glass is provided by the pair distribution function and bond angle distribution. In Fig. 2, the pair distribution functions, and bond angle distributions obtained for the different potentials at the 100 bar pressure route are
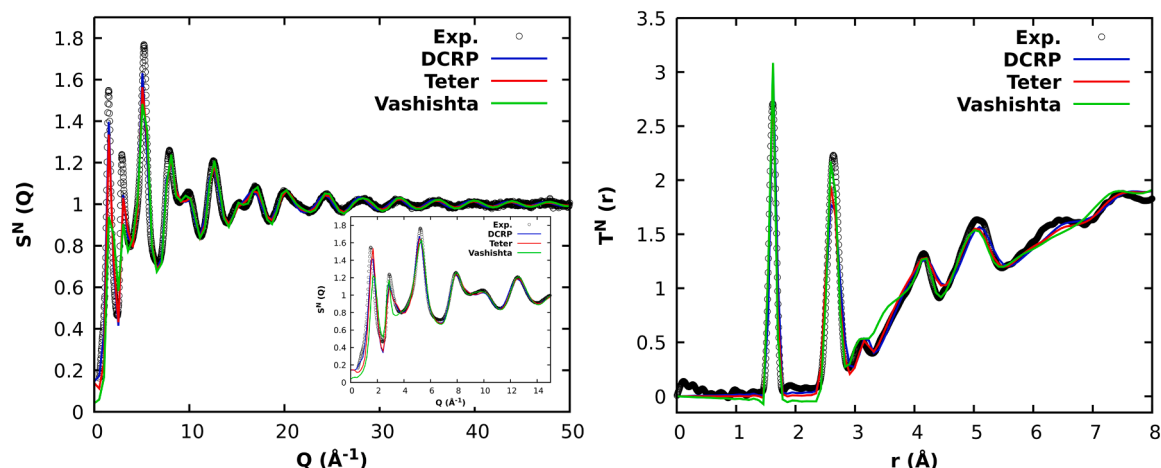
Fig. 1. Comparison of the structure factors (S^N (Q)) and total correlation functions (T^N (r)) obtained from the three potentials at the 1 bar pressure route compared to experimental results [41].
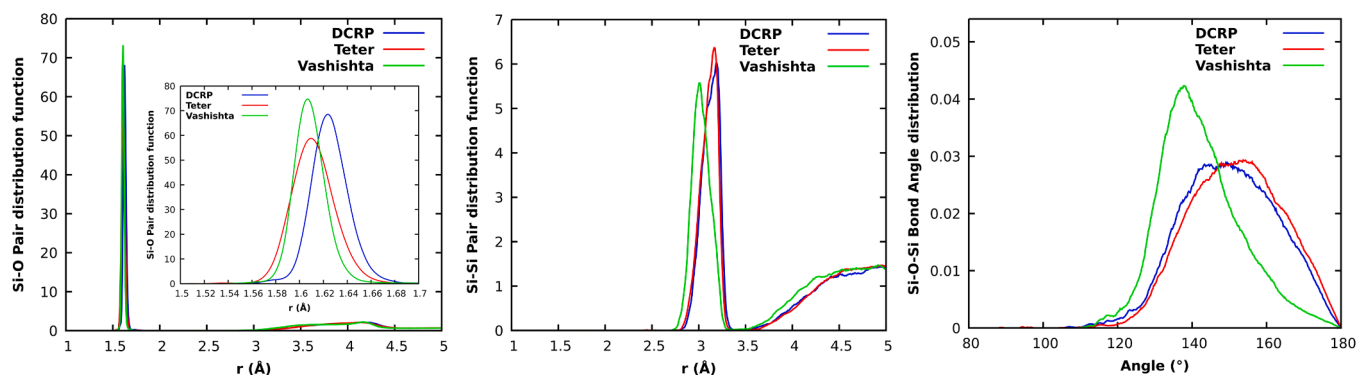

Fig. 2. Pair distribution functions of Si—O and Si—Si and bond angle distributions of Si—O—Si at the 100 bar pressure route.

shown for a structure with 15,972 atoms (See Fig S1 for additional information). In Table 2, the simulation results of bond angles are compared with experimental values.

The strongest peak position in the Si—O pair distribution function corresponds to the most probable value of the Si—O distance in the tetrahedra. The Si—O peak position yields values of 1.623 Å and 1.609 Å and 1.607 Å for DCRP, Teter and Vashishta, which are comparable to the most probable value of 1.59 Å obtained experimentally from nuclear magnetic resonance (NMR) spectroscopy [43].

On the other hand, the strongest peak position in Si—Si pair distribution function and the Si—O—Si bond angle distribution are related with the connectivity between tetrahedra. The Si—Si peak positions are located at 3.1858 Å and 3.1684 Å and 3.0094 Å for DCRP, Teter and Vashishta, respectively, which approach the experimental value of 3.061 Å [43]. Also, it is observed that DCRP, together with Teter potential, predict a Si—O—Si peak position in good agreement with the experimental value (see Table 2 for exact values).

Finally, it is remarkable that the lower Si—O—Si peak position and the significantly higher density with respect to the other two potentials obtained in Vashishta potential is consistent with different experimental works on the structural changes occurring in amorphous silica upon compaction, which reveal a progressive decrease in the Si—O—Si bond angle after performing permanent densification under hydrostatic pressure [44–47].

3.2. Structure size effects

As referred in the previous part, the structural information and elastic moduli are not expected to be subjected to fluctuations and converge to stable values once a minimum number of atoms 10^3 to 10^4 is considered. However, it is expected that size effects may play a role in the deformation and fracture behavior at considerably higher sizes. The deformation curves resulting from the different simulated structures using DCRP potential are shown in Fig. 3.

As observed from the deformation curves resulting from the different simulated structures, the elastic region is not significantly affected by the system size. However, after yield, a ductile tail is observed in some of the structures, which evidence structure size and geometry effects on breaking behavior of bulk silica structures during the tensile MD simulations. It is observed that the structures with the lowest aspect ratio, of 0.75, have a significant ductile tail, indicating a ductile fracture. For the 1.4 aspect ratio, only structures with the lowest cross sections, of 3.5 nm and 7.5 nm, show a substantial ductile tail in the stress-strain curve, indicating a ductile break. Finally, for the largest ratios, the breaking mode is clearly brittle, and the stress-strain becomes independent of the
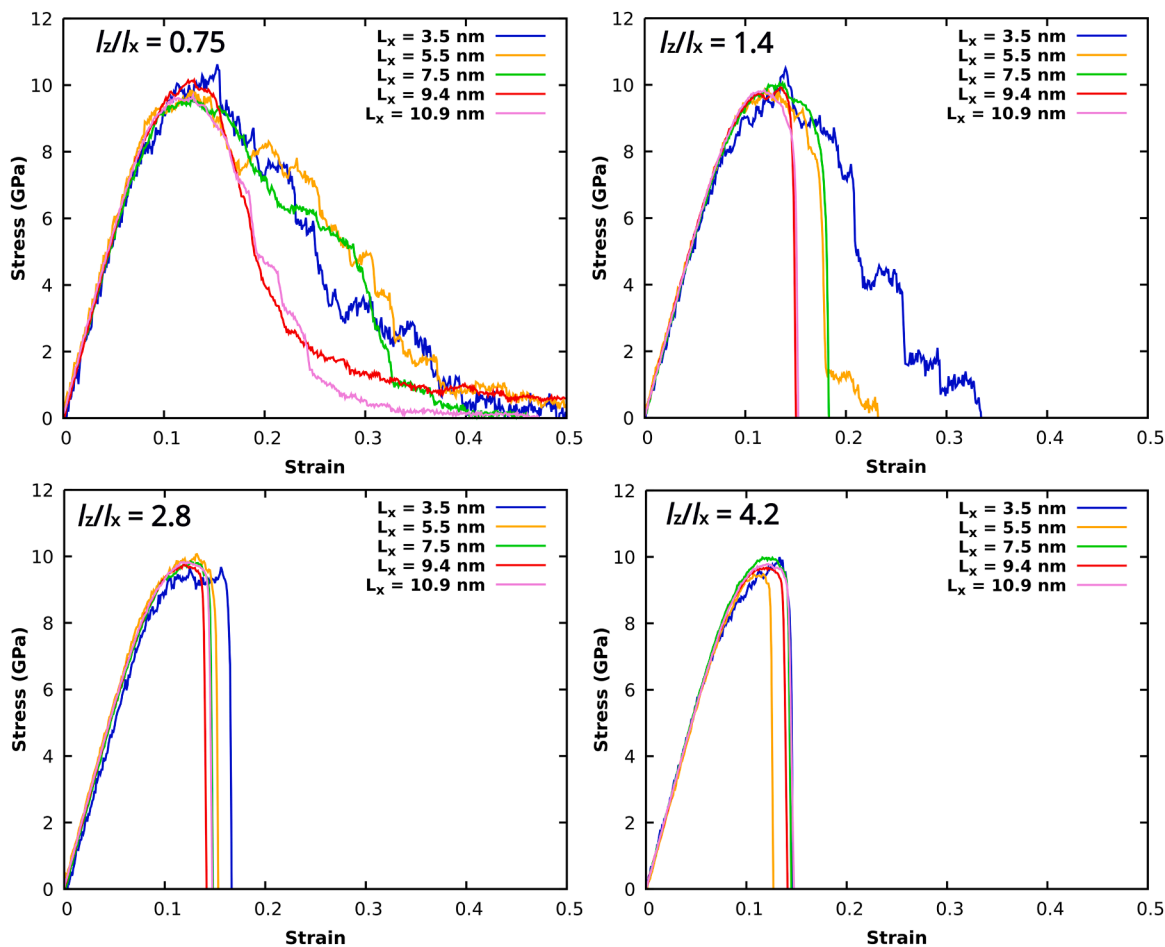
Table 2
Summary of the most probable (peak location) Si—O—Si angle and, in parentheses, the full width at half maximum at the 100 bar pressure route.

	Si—O—Si	
	Simulation	Experiments
DCRP	149.0° (34.0°)	149° (16°)[a], 147.7°[b]
Teter	153.7° (34.5°)	
Vashishta	137.8° (20.4°)	

[a] Ref. [42].
[b] Ref. [43].

Fig. 3. Stress-strain diagrams of amorphous silica structures produced using DCRP potential.

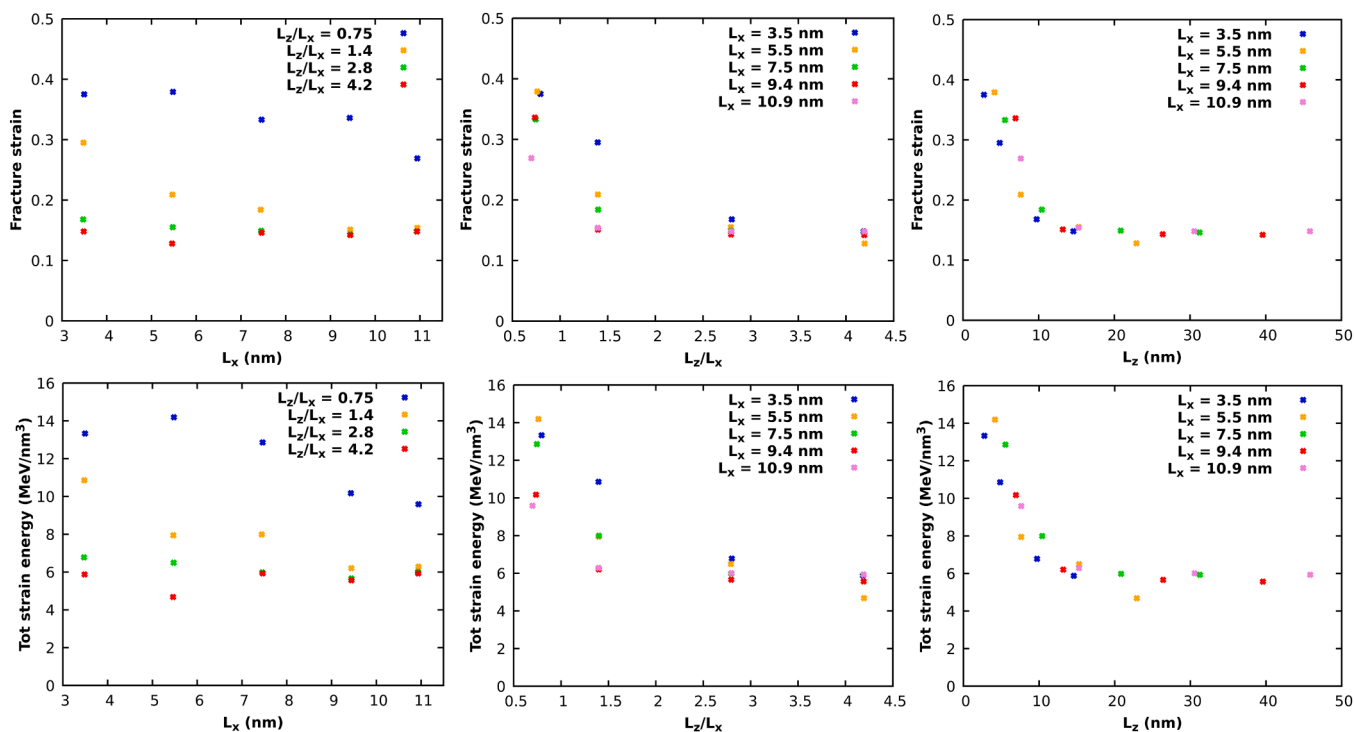**Fig. 4.** Fracture strain and total strain energy as a function of l_x, l_z/l_x and l_z for DCRP potential.

system size. In Fig S4 and S5, the stress-strain diagrams of the silica structures obtained using Teter and Vashishta potentials are shown.

Therefore, to quantitatively estimate the effect of the system size on the brittle-to-ductile transition, a more quantitative definition of ductility is considered. Experimentally, a common approach to quantify the ductility consists of measuring the change of the strain once the structure is subjected to fracture. Usually, an estimation of ductility can be performed from the deformation curve analysis using different approaches. One of them consists of estimating the ratio between the strain at failure and the recoverable elastic strain. In that approach, the recoverable elastic strain is calculated as the strain at the yield point, which is commonly estimated as the point which results in a plastic strain of 0.2 %. Another way to estimate the toughness is by calculating the area under the deformation curve.

In MD simulations of tensile tests of glass structures, the elastic region usually presents a strong non-linear behavior, which makes the yield point estimation ambiguous and overestimated. For this reason and the fact that in MD simulations the system response at strains below the strain at ultimate stress does not differ between the different structures, fracture strain and total strain energy can provide an accurate explanation of the relative change in the system ductility.

Therefore, in Fig. 4, the fracture strain and total strain energy as a function of l_x, l_z/l_x and l_z are shown for Vashishta potential.

In can be observed that both quantifications of structure ductility yield similar trends. On the other hand, as observed from the second fracture strain graph, fracture strain decreases as the aspect ratio increases, converging the points for all the cross lengths into the same value at 4.2. However, at aspect ratios of 0.7 and 1.25, structures with the shortest cross lengths show higher fracture strains, which can be observed at the 1.25 point, while the thicker ones are already closed to the final value at 4.2. This suggests that the l_x may not play a role in the structure breaking behavior. Instead, l_z length can be a more meaningful quantity for the study of the bulk ductility. Therefore, rather than focusing on the influence of the aspect ratio, fracture strain was studied against the l_z length along the deformation axis. As observed from the third graph, less dispersion is observed in the results as the fracture strain values resulting from the different cross section are closer to the trend of the curve when they are presented against the length l_z. Therefore, this suggests that the cross area does not have an effect in the deformation behavior. In turn, the breaking behavior is determined by the length l_z. As observed, fracture strain decreases from values in the order of 0.3–0.4 at lengths lower than 5 nm and reaches a constant value above a certain length. A brittle to ductile transition can be observed at lengths around 10 nm for DCRP potential. In Fig S6 and 7, the fracture strain and total strain energy are shown for DCRP and Teter potentials. It can be observed a similar behavior.

In order to compare the brittle to ductile transition length for the different potentials, the cross area and aspect ratio are disregarded and fracture strain and total strain energy against the l_z length is compared for the three potentials, as shown in Fig. 5.

It can be seen that Teter and Vashishta potentials show a brittle to ductile transition at a similar length as DCRP potential, which is located at approximately 10 nm. Such threshold length has also been obtained in previous works on MD simulations of uniaxial tensile tests using other potentials as BKS [12] and SHIK [18] potentials.

To understand the size effect, we propose an energy procedure similar to Yuan et al. approach, involving the computation of fracture surface energies and elastic strain energies [12]. Following Section 2.4, a prior analysis of the fracture surface energy is conducted through the three potentials. The unrelaxed fracture surface energy $FSE_{relaxed}$ and $FSE_{unrelaxed}$ were computed for the different configurations and potentials (see Table S3). It can be observed that $FSE_{unrelaxed}$ yields higher values, as it defines an uper bound for ideal fracture with perfectly flat surfaces. Interestingly, $FSE_{unrelaxed}$ can provide a more exact estimation of the energy released immediately after failure provided that there a perfectly brittle fracture takes place in the structure. Therefore, in the analysis, the unrelaxed values where considered. On the other hand, the elastic strain energy, ESE, was calculated following Eq. (2).

In Fig. 6, $FSE_{unrelaxed}$ versus cross area, ESE versus volume and ESE/ FSE ratio versus l_z axis length are shown for DCRP potential. As observed in the graphs, fracture surface energy is proportional to the structure cross area. On the other hand, elastic strain energy linearly increases with the volume of the system. Therefore, if we consider the elastic strain energy to fracture surface energy ratio and the structure length, the previous relations result in a linear increase, as observed in Fig. 6 (right).

To correlate such energy analysis with the structure ductility, the fracture strain against ESE/FSE ratio is shown in Fig. 7 for DCRP potential.

It is seen that ESE/FSE values lower than 1 lead to high fracture strains, suggesting a ductile fracture in this region, which does not depend on the cross length. However, fracture strain decreases as the ESE/FSE ratio increases and it saturates at ESE/FSE ratios closed to 1. This suggests that an ESE/FSE ratio of 1 provides a ductile to brittle transition for DCRP potential. If we observe the graph simultaneously with the ESE/FSE to l_z graph, all the points corresponding to ESE/FSE lower than 1 in the fracture strain against energy ratio graph, which lead to ductile behavior, correspond to structures with l_z lengths lower than a value which is around 10 nm, as seen from the ESE/FSE against l_z graph. On the other hand, points with ESE/FSE values higher than 1, which lead to brittle behavior, correspond to structures with l_z lengths higher than 10 nm.

In order to assess whether the above conclusion can be extended to Teter and Vashishta potentials, in Fig. 8 ESE/FSE versus l_z and fracture strain versus ESE/FSE for the three potentials is shown.

As observed, the brittle to ductile transition at ESE/FSE of 1 can also be extended to DCRP and Teter potentials. Therefore, if we generalize, we can conclude that tensile bulk glass MD simulations of structures with ESE/FSE ratios lower than one will lead to a ductile breaking behavior, while structures with ESE/FSE ratios higher than one will
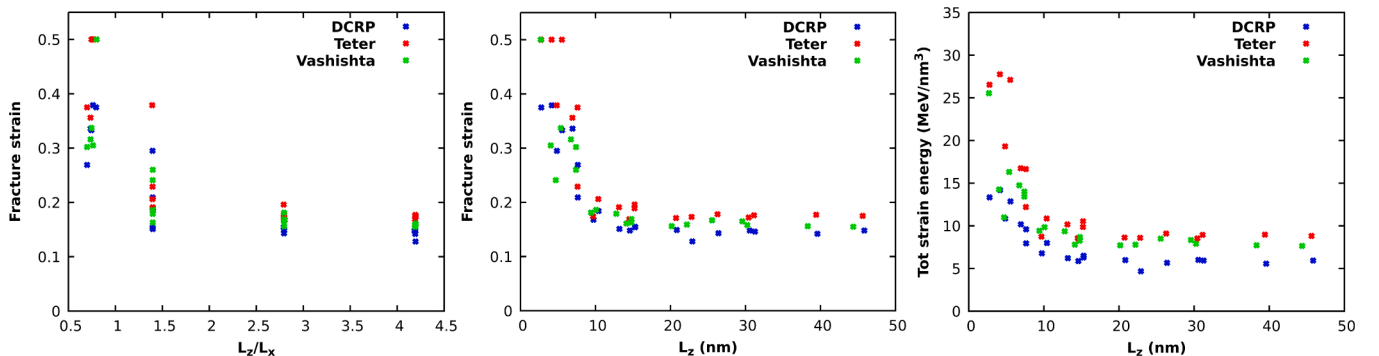

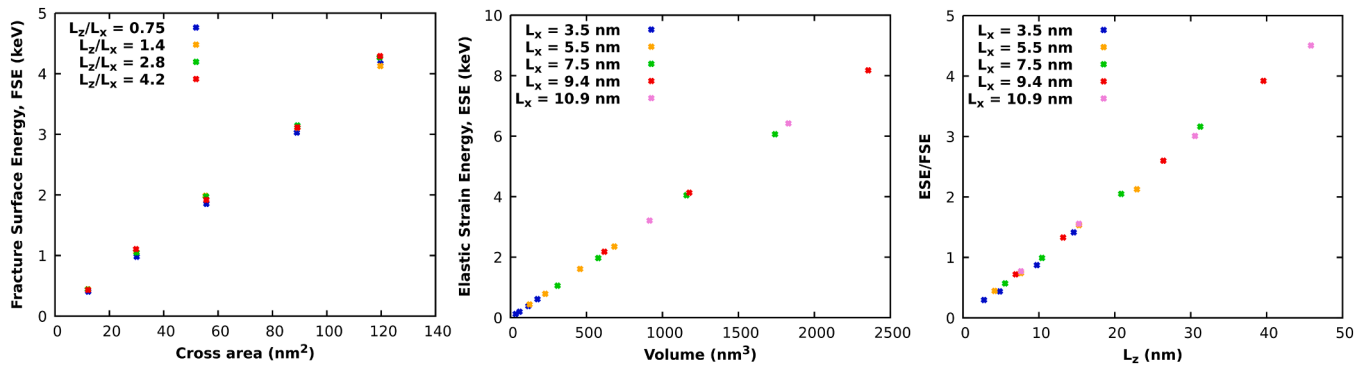**Fig. 5.** Fracture strain as a function of l_z/l_x and l_z for DCRP, Teter and Vashishta potentials.

Fig. 6. *FSE_unrelaxed* versus cross area, ESE versus volume and ESE/FSE ratio versus l_z axis length.
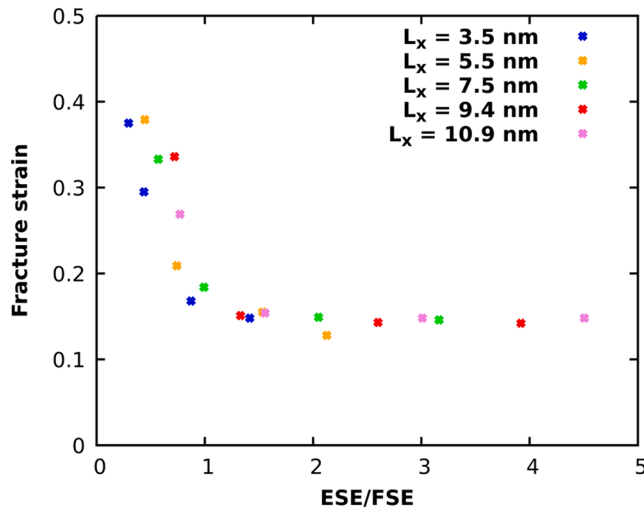

Fig. 7. Fracture strain against ESE/FSE ratio for DCRP potential.

have a brittle behavior. Therefore, as the ESE/FSE ratio linearly increases with the structure length along the deformation axis, a threshold length for ductile to brittle transition can be obtained from direct calculations on the slope of ESE/FSE against l_z length, as the length corresponding to a value of ESE/FSE of 1. For pure amorphous silica bulk glass simulated with the Vashishta, DCRP and Teter potentials, the slope of the ESE/FSE against l_z length curve has been shown to be similar. This explains the fact that the threshold takes place at the same length of

around 10 nm.

A more analytical analysis can be performed considering the analytical expressions for fracture surface energy and elastic strain energy, from Eqs. (5) and (6), respectively. In such conditions, an ESE/FSE ratio of 1 would result in a minimum length for brittle behavior of:

$$l_{z,\min} = \frac{4\gamma_f}{E\varepsilon^2} \qquad (7)$$

Where γ_f is the fracture surface energy, E the Young's Modulus and ε_l the elastic strain energy.

In table S4, the $\gamma_{f,\text{relaxed}}$ and $\gamma_{f,\text{unrelaxed}}$ are shown. The average values of $\gamma_{f,\text{unrelaxed}}$ are 2.81 J/m^2, 5.44 J/m^2 and 3.75 J/m^2, for DCRP, Teter and Vashishta, respectively. For $\gamma_{f,\text{relaxed}}$, simulations yield values of 2.04 J/m^2, 3.31 J/m^2 and 2.72 J/m^2, for DCRP, Teter and Vashishta, respectively. Shi et al. obtained values of $\gamma_{f,\text{unrelaxed}}$ and $\gamma_{f,\text{relaxed}}$ of 3.5 J/m^2 and 2.5 J/m^2 respectively, using BKS potential [23].

Considering the values of $\gamma_{f,\text{unrelaxed}}$ and the Young's Modulus values obtained from a fit of the stress-strain curve at the 0–3 % strain range, minimum lengths for brittle behavior of 10.22 nm, 9.54 nm and 11.96 nm are obtained for DCRP, Teter and Vashishta, respectively. Therefore, the energy considerations lead to similar conclusions about the minimum length for brittle behavior through the different potentials considered. Accordingly, the energy approach was validated through the different potentials and it was shown that all of them show a ductile-to-brittle transition at length values around 10 nm. Such result was finally supported by calculations using analytical results based on the γ_f, E and ε_l obtained using MD simulations, which show reasonably similar values of minimum lengths.
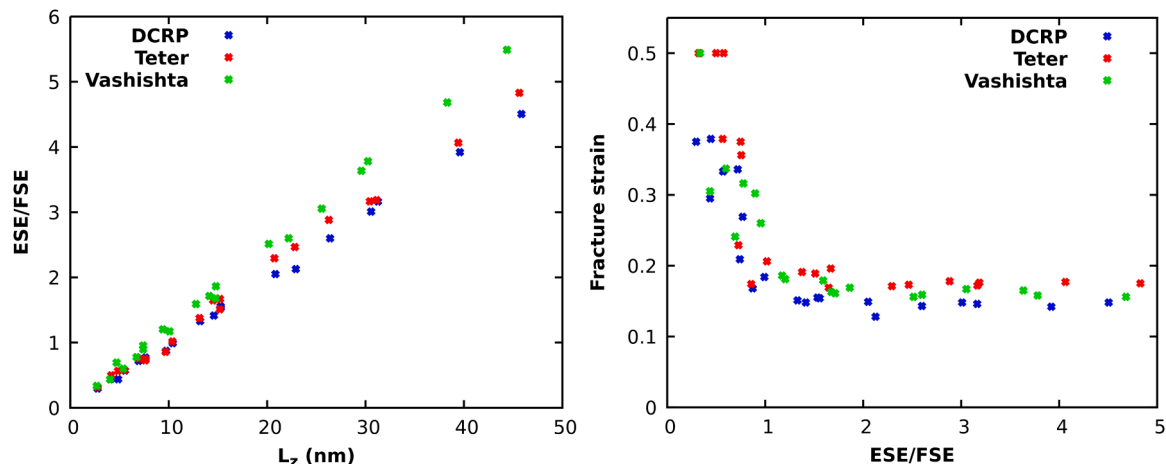

Fig. 8. ESE/FSE versus l_z and fracture strain versus ESE/FSE for DCRP, Teter and Vashishta potentials.

3.3. Elastic moduli and mechanical properties

In this section, the elastic moduli and mechanical properties (i.e. ultimate strength and fracture strain) are compared against results obtained by other researchers using other potentials and experimental results of mechanical properties of amorphous silica glass. For this purpose, the elastic moduli are calculated following the static method of energy minimization and compared to the Young's modulus obtained from the analysis of the linear region of the stress-strain curve. On the other hand, the ultimate strength and fracture strain are obtained based on the stress-strain curves.

3.3.1. Elastic moduli analysis

The role of structure size in the elastic moduli obtained in MD simulations using the static method has been previously studied in sodium borosilicate glasses [40]. The elastic moduli values were shown to plateau and become stable at system sizes larger than around 10^3–10^4 atoms [40]. On the other hand, as shown in the previous section, the deformation curves in the elastic range do not show appreciable variation with the system size, which confirms that structure size has a neglectable effect on elastic moduli. Also, once the system size is larger than several thousands of atoms, the elastic curve becomes smoother, indicating that a higher statistical significance is obtained. Therefore, for the computation of the elastic moduli using the static method involving energy minimization, a structure of 15,972 atoms was considered. Such elastic moduli analysis of this section is performed considering the melt-quench structures generated using the 100 bar pressure route.

In order to study the effect of the deformation range on the elastic response, different values of strains of 0.01 %, 0.1 %, 0.5 %, 1 %, 5 %, and 10 % were applied in *x, y, z, xy, yz* and *xz* directions and the C_{11}, C_{22} and C_{33} components of the stiffness matrix were calculated for each of the strains. The results are plot in Fig S2. Ideally, as a result of glass isotropicity, the three constants should yield equal values. However, at low strains, a high dispersion is observed between the constants. As the deformation strain increases, the three values converge and start to decrease when the applied strain is higher than 0.5 %, because of the departure from the linear region. Consequently, a deformation of 0.5 % was established for the calculations of the components of the stiffness matrix.

Once obtained the components of the stiffness matrix, the bulk (*B*), shear (*G*) and Young's modulus (*E*) were calculated following Voigt, Reuss and Hill average methods (see Table 3). As shown in Table S5, no significant difference is noticed between Voigt and Reuss methods. Therefore, the elastic moduli presented in this work are based on Hill approximation.

As explained in Section 2.2, the Young's Modulus was also computed from the deformation curve in the elastic region. The Young's Modulus values evaluated from the fit of the deformation curve at different fitting range are shown in Table S6. It is observed that the Young's Modulus is not constant over the different fitting ranges, confirming that the tested potentials also result in a non-linear behavior. Conversely, for DCRP and Vashishta, it decreases when higher fitting ranges are used, while for Teter increases.

To support such predictions, in Fig S3, the stress-strain diagrams and the tangent modulus fit in the strain range from 0 to 6 % are compared for the three potentials and structures with 15,972 and 383,328 atoms and, in Table S7, the 3rd order polynomial fit coefficients, including the zero strain Young's Modulus E_0, are shown. For Teter, an increase with strain is observed, which is in line with the predictions from other works using other potentials, as reported in Section 2.2 [12,15,18,21,39]. Conversely, for DCRP and Vashishta, an opposite trend is observed. In this work, in order to compare the results against that obtained using the static method, the Young's Modulus values in the 0 to 3 % strain range are considered.

3.3.2. Mechanical properties comparison

Having detailed the parameters for obtaining the elastic modulus using both computation methods, the mechanical properties resulting from the studied potentials are compared to that obtained from other MD simulation works and experimental values of amorphous silica glass.

The fracture strain values obtained through MD simulations, at sizes above the brittle to ductile transition, together with the ultimate strengths, can be used as predictors of the mechanical properties of the macroscopically brittle glass. Therefore, the mechanical properties from the stress-strain curve are obtained from the largest simulated sample of 383,328 atoms. As a result, such values can be directly compared to experimental values of mechanical properties, as explained in the following section.

In Table 3, the mechanical properties obtained using the studied potentials and different pressure routes are compared against the results obtained from other works using other potentials, and experimental results.

First, it can be noticed that the Young's modulus values obtained from direct analysis of the stress-strain curve are reasonably different compared to that obtained from energy minimization. Such difference can be associated to the different computation approach, where the former is based on stresses while the latter is based on energies.

On the other hand, it is observed that the studied potentials yield higher values of elastic properties compared with experimental results, which could be explained on the view of the higher density obtained

Table 3

Density, elastic moduli (bulk modulus B, shear modulus G, Young's modulus E), Poisson's ratio ν, failure strain ε_f and stress σ_f, compared to other potentials and experiments. In parentheses, the Young's Modulus obtained from a fit of the stress-strain curve in the 0 % to 3 % strain range is presented.

	ρ / g·cm^{-3}	B / GPa	G / GPa	E / GPa	ν	ε_f	σ_f / GPa
Vash (100 bar)	2.565	84.7	57.1	139.8 (125.4)	0.22	12.9	12.3
Vash (1 bar)	2.551	80.2	53.9	132.1	0.23	–	–
DCRP (100 bar)	2.327	68.3	48.3	117.2 (109.9)	0.21	12.2	9.78
DCRP (1 bar)	2.205	53.7	31.2	78.5	0.26	–	–
Teter (100 bar)	2.359	62.4	42.0	102.8 (101.4)	0.23	15.3	13.2
Teter (1 bar)	2.329	56.4	38.1	93.2	0.22	–	–
BKS	2.241[a]	52.3[a]	35.0[a]	85.8[a]	0.226[a]	17.18[a]	17.65[a]
ReaxFF	2.14[b]	–	–	58[b]	–	40[b]	22[b]
Pedone potential	2.26[c]	42.5[c]	27.4[c]	69.9[c]	0.277[c]	15.3[c]	10.8[c]
SHIK	2.221[a]	40.8[a]	29.9[a]	72.1[a]	0.205[a]	16.89[a]	12.84[a]
Experimental	2.201[d]	36.5[d]	31.3[d]	72.9[d]	0.165[d]	18[e]	11–14[f]

[a] Ref. [18].
[b] Ref. [20].
[c] Ref. [15].
[d] Ref. [24].
[e] Ref. [6].
[f] Ref. [46].

with all the potentials with respect to the experimental value of 2.2 g/cm^3. Indeed, Vashishta potential, with a higher density compared to DCRP and Teter, shows also significantly higher Young's Modulus compared to that of the other potentials (see Table 3). These results are consistent with the experimentally observed correlation between the elastic moduli and the glass density, where more densified samples usually result in higher elastic moduli, as reported through several studies on elastic moduli of permanently densified silica glass upon compression using acoustic waves [4,44,46]. Indeed, higher density using the ramping pressure leads to higher densities and elastic moduli while the constant 1 bar constant pressure cooling leads to densities and mechanical properties closer to experiments. Generally, this trend can be also assessed when comparing different results from different works on MD simulations of uniaxial tensile tests and elastic properties calculations using different potentials, where potentials yielding lower densities, closer to the experimental value, also result in Young's Modulus more comparable to experimental results (see Table 2). Accordingly, pairwise empirical potential developed by Pedone et al., leading to a density of 2.19 g/cm^3, has provided a more accurate modelling of the mechanical properties, obtaining a Young's Modulus value of 69.9 GPa from MD tensile deformation tests of silica glass [15]. Also, Zhang et al. performed MD simulations of uniaxial tensile tests using reaxFF potential obtaining a density of 2.24 g/cm3 and Young's Modulus of 58 GPa. SHIK potential, developed by Sundararaman et al., has been also proved as a reliable potential for simulating the mechanical properties, obtaining densities and Young's Modulus of 2.22 g/cm^3 and 72.1 GPa, respectively. BKS potential also resulted in densities and elastic moduli comparable to experiments [12,13,18], but a more significant dependence on the short range cutoff of the potential was noticed [12,13]. Accordingly, Sundararaman et al. obtained densities and Young's Modulus of 2.24 g/cm^3 and 84 GPa, respectively, at a cutoff of 5.5 Å, varying to 2.34 g/cm^3 and 72 GPa when the cutoff is increased up to 10 Å [13].

It is also observed that DCRP predicts an ultimate strength of 9.78 GPa, which is slightly lower compared to the experimental intrinsic strength, presumably in the range between 11 GPa and 14 GPa, obtained for silica fibers under ultra-high vacuum conditions [46]. Conversely, Vashishta and Teter potentials predict ultimate strengths more in agreement with the experimental value. Results similar to experiments were also obtained in previous works from Pedone and SHIK potentials.

For the fracture strain, DCRP and Vashishta predict 12.2 % and 12.9 %, which are lower compared to Teter potential and other works on other potentials, which range between 15 % and 18 %. While failure strains in excess of 18 % were achieved reported experimentally in the nanoscale, glass ductility has been a matter of more controversy as it is considerably affected by size effects.

4. Conclusions

The aim of this work has been to analyze the size effects on deformation behavior of bulk amorphous silica glass in uniaxial tensile testing using classical MD simulations. Special emphasis was laid on the on the ductility, and its dependence on the interaction potentials, through the use of the DCRP, Teter and Vashishta potential. The mechanical properties resulting from the different potentials were estimated and compared against other results from other potentials existing in the literature and experimental results.

In agreement with previous studies, an important role of simulation cell size on fracture behavior was observed for the three potentials considered. It was found that the length along the deformation axis was the most relevant factor involved in structure size effects, while no significant effects of the system cross section on the breaking behavior was noticed in any of the potentials. To sustain such conclusions, an energy approach was applied to the three potentials, and it was shown that, while the different potentials show different fracture surface energies and elastic energies, they all agree in that the necessary condition

for a potential to show brittle behavior is that the fracture surface energy has to overcome the elastic strain energy stored in the glass before fracture failure can take place. The results also show that the three potentials show a reasonable agreement in the minimum required length for the ductile to brittle transition, which was determined to be located at around 10 nm for amorphous silica glass.

Such results were supported by a more analytical argument, which involves the computation of the minimum length for brittle behavior using glass properties based on the fracture surface energy γ_f, the Young's Modulus E and the elastic strain energy ε_l. The calculated minimum lengths obtained from the different potentials result in similar values, which are closed to 10 nm. The consistency of the results with the energy analysis, combined with the analytical expression through the different potentials, not only reassert the validity of such approach, but also facilitate the prediction of the size effects on fracture behavior in MD simulations of more complex systems, involving network modifier cations, such as sodium, from the computation of accessible glass properties, therefore reducing computational efforts.

CRediT authorship contribution statement

Raúl Barciela: Writing – original draft, Investigation, Formal analysis. **Thiruvilla S. Mahadevan:** Software, Methodology. **Félix Quintero:** Writing – review & editing, Formal analysis, Conceptualization. **Juan Pou:** Writing – review & editing, Supervision, Project administration. **Jincheng Du:** Writing – review & editing, Methodology, Conceptualization.

Declaration of competing interest

The authors declare that they have no known competing financial interests or personal relationships that could have appeared to influence the work reported in this paper.

Data availability

No data was used for the research described in the article.

Acknowledgements

Supplementary materials

Supplementary material associated with this article can be found, in the online version, at doi:10.1016/j.jnoncrysol.2024.122935.

References

[1] K. Zheng, C. Wang, Y.Q. Cheng, Y. Yue, X. Han, Z. Zhang, Z. Shan, S.X. Mao, M. Ye, Y. Yin, E. Ma, Electron-beam-assisted superplastic shaping of nanoscale amorphous silica, Nat. Commun. 1 (2010) 1–8, https://doi.org/10.1038/ncomms1021.

[2] S.G. Kang, K. Jeong, J. Paeng, W. Jeong, S. Han, J.P. Ahn, S. Boles, H.N. Han, I. S. Choi, Athermal glass work at the nanoscale: engineered electron-beam-induced viscoplasticity for mechanical shaping of brittle amorphous silica, Acta Mater. 238 (2022), https://doi.org/10.1016/j.actamat.2022.118203.

[3] S. Bruns, C. Minnert, L. Pethö, J. Michler, K. Durst, Room temperature viscous flow of amorphous silica induced by electron beam irradiation, Adv. Sci. 10 (2023) 1–9, https://doi.org/10.1002/advs.202205237.

[4] M. Guerette, M.R. Ackerson, J. Thomas, F. Yuan, E.B. Watson, D. Walker, L. Huang, Structure and properties of silica glass densified in cold compression and hot compression, Sci. Rep. 5 (2015) 1–10, https://doi.org/10.1038/srep15343.

[5] F. Célarié, S. Prades, D. Bonamy, L. Ferrero, E. Bouchaud, C. Guillot, C. Marlière, Glass breaks like metal, but at the nanometer scale, Phys. Rev. Lett. 90 (2003) 4, https://doi.org/10.1103/PhysRevLett.90.075504.

[6] J. Luo, J. Wang, E. Bitzek, J.Y. Huang, H. Zheng, L. Tong, Q. Yang, J. Li, S.X. Mao, Size-dependent brittle-to-ductile transition in silica glass nanofibers, Nano Lett. 16 (2016) 105–113, https://doi.org/10.1021/acs.nanolett.5b03070.

[7] L. Wondraczek, E. Bouchbinder, A. Ehrlicher, J.C. Mauro, R. Sajzew, M. M. Smedskjaer, Advancing the mechanical performance of glasses: perspectives and challenges, Adv. Mater. (2022) 34, https://doi.org/10.1002/adma.202109029.

[8] L. Deng, J. Du, Development of boron oxide potentials for computer simulations of multicomponent oxide glasses, J. Am. Ceram. Soc. 102 (2019) 2482–2505, https://doi.org/10.1111/jace.16082.

[9] L.-H. Kieu, J.-M. Delaye, L. Cormier, C. Stolz, Development of empirical potentials for sodium borosilicate glass systems, J. Non. Cryst. Solids 357 (2011) 3313–3321, https://doi.org/10.1016/j.jnoncrysol.2011.05.024.

[10] M. Wang, N.M. Anoop Krishnan, B. Wang, M.M. Smedskjaer, J.C. Mauro, M. Bauchy, A new transferable interatomic potential for molecular dynamics simulations of borosilicate glasses, J. Non. Cryst. Solids 498 (2018) 294–304, https://doi.org/10.1016/j.jnoncrysol.2018.04.063.

[11] P. Vashishta, R.K. Kalia, J.P. Rino, I.I. Ebbsjö, Interaction potential for SiO2: a molecular-dynamics study of structural correlations, Phys. Rev. B. Condens. Matter 41 (1990) 12197–12209, https://doi.org/10.1103/physrevb.41.12197.

[12] F. Yuan, L. Huang, Molecular dynamics simulation of amorphous silica under uniaxial tension: from bulk to nanowire, J. Non. Cryst. Solids 358 (2012) 3481–3487, https://doi.org/10.1016/j.jnoncrysol.2012.05.021.

[13] S. Sundararaman, W.Y. Ching, L. Huang, Mechanical properties of silica glass predicted by a pair-wise potential in molecular dynamics simulations, J. Non. Cryst. Solids 445-446 (2016) 102–109, https://doi.org/10.1016/j.jnoncrysol.2016.05.012.

[14] A. Pedone, G. Malavasi, M.C. Menziani, A.N. Cormack, U. Segre, A new self-consistent empirical interatomic potential model for oxides, silicates, and silica-based glasses, J. Phys. Chem. B 110 (2006) 11780–11795, https://doi.org/10.1021/jp0611018.

[15] A.N. Cormack, U. Segre, M.C. Menziani, G. Malavasi, A. Pedone, Molecular dynamics studies of stress−strain behavior of silica glass under a tensile load, Chem. Mater. 20 (2008) 4356–4366, https://doi.org/10.1021/cm800413v.

[16] A. Pedone, M.C. Menziani, A.N. Cormack, Dynamics of fracture in silica and soda-silicate glasses: from bulk materials to nanowires, J. Phys. Chem. C 119 (2015) 25499–25507, https://doi.org/10.1021/acs.jpcc.5b08657.

[17] S. Sundararaman, L. Huang, S. Ispas, W. Kob, New optimization scheme to obtain interaction potentials for oxide glasses, J. Chem. Phys. 148 (2018) 194504, https://doi.org/10.1063/1.5023707.

[18] Z. Zhang, S. Ispas, W. Kob, The critical role of the interaction potential and simulation protocol for the structural and mechanical properties of sodosilicate glasses, J. Non. Cryst. Solids 532 (2020) 119895, https://doi.org/10.1016/j.jnoncrysol.2020.119895.

[19] A.C.T. van Duin, A. Strachan, S. Stewman, Q. Zhang, X. Xu, W.A. Goddard, ReaxFFSiO reactive force field for silicon and silicon oxide systems, J. Phys. Chem. A 107 (2003) 3803–3811, https://doi.org/10.1021/jp0276303.

[20] C. Zhang, F. Duan, Q. Liu, Size effects on the fracture behavior of amorphous silica nanowires, Comput. Mater. Sci. 99 (2015) 138–144, https://doi.org/10.1016/j.commatsci.2014.12.020.

[21] P.K. Gupta, C.R. Kurkjian, Intrinsic failure and non-linear elastic behavior of glasses, J. Non. Cryst. Solids 351 (2005) 2324–2328, https://doi.org/10.1016/j.jnoncrysol.2005.05.029.

[22] B. Wang, Y. Yu, Y.J. Lee, M. Bauchy, Intrinsic nano-ductility of glasses: the critical role of composition, Front. Mater. 2 (2015) 1–9, https://doi.org/10.3389/fmats.2015.00011.

[23] Y. Shi, J. Luo, F. Yuan, L. Huang, Intrinsic ductility of glassy solids, J. Appl. Phys. (2014) 115, https://doi.org/10.1063/1.4862959.

[24] N.P. Bansal, R.H. Doremus, Handbook of glass properties, Handb. Glas. Prop. (2013) 1–680, https://doi.org/10.1016/C2009-0-21785-5.

[25] F.-X. Coudert, Failure to reproduce the results of "A new transferable interatomic potential for molecular dynamics simulations of borosilicate glasses," J. Non. Cryst. Solids 615 (2023) 122423, https://doi.org/10.1016/j.jnoncrysol.2023.122423.

[26] J. Du, A.N. Cormack, The medium range structure of sodium silicate glasses: a molecular dynamics simulation, J. Non. Cryst. Solids 349 (2004) 66–79, https://doi.org/10.1016/j.jnoncrysol.2004.08.264.

[27] J. Kalahe, M. Ono, S. Urata, J. Du, Composition dependence of the atomic structures and properties of sodium aluminosilicate glasses: molecular dynamics simulations with reactive and nonreactive potentials, J. Phys. Chem. B 126 (2022) 5326–5342, https://doi.org/10.1021/acs.jpcb.2c02292.

[28] J. Kalahe, Y. Onodera, Y. Takimoto, H. Hijiya, M. Ono, K. Miyatani, S. Kohara, S. Urata, J. Du, Influence of interatomic potential and simulation procedures on the structures and properties of sodium aluminosilicate glasses from molecular dynamics simulations, J. Non. Cryst. Solids 588 (2022), https://doi.org/10.1016/j.jnoncrysol.2022.121639.

[29] S.H. Garofalini, Dissociative chemisorption of water onto silica surfaces and formation of hydronium ions, J. Phys. Chem. C 112 (2008) 5694, https://doi.org/10.1021/jp8015134.

[30] T. Mahadevan, A. Baroni, M. Taron, S. Gin, J. Du, J.-M. Delaye, Development of potentials for molecular dynamics simulations of dry and hydrated calcium aluminosilicate glasses by force matching and refinement, J. Non. Cryst. Solids 592 (2022) 121746, https://doi.org/10.1016/j.jnoncrysol.2022.121746.

[31] T.S. Mahadevan, W. Sun, J. Du, Development of water reactive potentials for sodium silicate glasses, J. Phys. Chem. B 123 (2019) 4452–4461, https://doi.org/10.1021/acs.jpcb.9b02216.

[32] S.M. Wiederhorn, Influence of water vapor on crack propagation in soda-lime glass, J. Am. Ceram. Soc. 50 (1967) 407–414, https://doi.org/10.1111/j.1151-2916.1967.tb15145.x.

[33] S.M. Wiederhorn, L.H. Bolz, Stress corrosion and static fatigue of glass, J. Am. Ceram. Soc. 53 (1970) 543–548, https://doi.org/10.1111/j.1151-2916.1970.tb15962.x.

[34] S. Plimpton, Fast parallel algorithms for short-range molecular dynamics, J. Comput. Phys. 117 (1995) 1–19, https://doi.org/10.1006/jcph.1995.1039.

[35] S. Nosé, A unified formulation of the constant temperature molecular dynamics methods, J. Chem. Phys. 81 (1984) 511–519, https://doi.org/10.1063/1.447334.

[36] W.G. Hoover, Canonical dynamics: equilibrium phase-space distributions, Phys. Rev. A 31 (1985) 1695–1697, https://doi.org/10.1103/PhysRevA.31.1695.

[37] W.G. Hoover, Constant-pressure equations of motion, Phys. Rev. A 34 (1986) 2499–2500, https://doi.org/10.1103/PhysRevA.34.2499.

[38] R. Hill, The elastic behaviour of a crystalline aggregate, Proc. Phys. Soc. Sect. A 65 (1952) 349, https://doi.org/10.1088/0370-1298/65/5/307.

[39] Z. Zhang, S. Ispas, W. Kob, Origin of the non-linear elastic behavior of silicate glasses, Acta Mater. 231 (2022) 117855, https://doi.org/10.1016/j.actamat.2022.117855.

[40] L. Deng, J. Du, Effects of system size and cooling rate on the structure and properties of sodium borosilicate glasses from molecular dynamics simulations, J. Chem. Phys. 148 (2018), https://doi.org/10.1063/1.5007083.

[41] D.I. Grimley, A.C. Wright, R.N. Sinclair, Neutron scattering from vitreous silica IV. Time-of-flight diffraction, J. Non. Cryst. Solids 119 (1990) 49–64, https://doi.org/10.1016/0022-3093(90)90240-M.

[42] W.J. Malfait, W.E. Halter, R. Verel, 29Si NMR spectroscopy of silica glass: T1 relaxation and constraints on the Si–O–Si bond angle distribution, Chem. Geol. 256 (2008) 269–277, https://doi.org/10.1016/j.chemgeo.2008.06.048.

[43] N.M. Trease, T.M. Clark, P.J. Grandinetti, J.F. Stebbins, S. Sen, Bond length-bond angle correlation in densified silica - results from 17O NMR spectroscopy, J. Chem. Phys. (2017) 146, https://doi.org/10.1063/1.4983041.

[44] T. Deschamps, A. Kassir-Bodon, C. Sonneville, J. Margueritat, C. Martinet, D. De Ligny, A. Mermet, B. Champagnon, Permanent densification of compressed silica glass: a Raman-density calibration curve, J. Phys. Condens. Matter (2013) 25, https://doi.org/10.1088/0953-8984/25/2/025402.

[45] T. Deschamps, J. Margueritat, C. Martinet, A. Mermet, B. Champagnon, Elastic moduli of permanently densified silica glasses, Sci. Rep. 4 (2014) 1–7, https://doi.org/10.1038/srep07193.

[46] C.R. Kurkjian, P.K. Gupta, R.K. Brow, N. Lower, The intrinsic strength and fatigue of oxide glasses, J. Non. Cryst. Solids 316 (2003) 114–124, https://doi.org/10.1016/S0022-3093(02)01943-9.

[47] N. Sun, Z. Mao, X. Zhang, S.N. Tkachev, J.F. Lin, Hot dense silica glass with ultrahigh elastic moduli, Sci. Rep. 12 (2022) 1–11, https://doi.org/10.1038/s41598-022-18062-6.